We are IntechOpen, the world's leading publisher of Open Access books
Built by scientists, for scientists

6,900
Open access books available

186,000
International authors and editors

200M
Downloads

154
Countries delivered to

Our authors are among the

TOP 1%
most cited scientists

12.2%
Contributors from top 500 universities

CLARIVATE ANALYTICS
BOOK CITATION INDEX
INDEXED

WEB OF SCIENCE™

Selection of our books indexed in the Book Citation Index
in Web of Science™ Core Collection (BKCI)

Interested in publishing with us?
Contact book.department@intechopen.com

Numbers displayed above are based on latest data collected.
For more information visit www.intechopen.com

In Situ Transmission Electron Microscopy Studies in Gas/Liquid Environment

Fan Wu and Nan Yao

Abstract

Conventional transmission electron microscopy (TEM) typically operates under high vacuum conditions. However, *in situ* investigation under real-world conditions other than vacuum, such as gaseous or liquidus environment, is essential to obtain practical information for materials including catalysts, fuel cells, biological molecules, lithium ion batteries, etc. Therefore, the ability to study gas/liquid–solid interactions with atomic resolution under ambient conditions in TEM promises new insights into the growth, properties, and functionality of nanomaterials. Different platforms have been developed for *in situ* TEM observations in ambient environment and can be classified into two categories: open-cell configuration and sealed gas/liquid cell configuration. The sealed cell technique has various advantages over the open-cell approach. This chapter serves as a review of windowed gas/liquid cells for *in situ* TEM observations.

Keywords: *In situ* TEM, sealed gas cell, sealed liquid cell, lithium ion battery, open-cell configuration

1. Introduction

Transmission electron microscopy (TEM) is one of the most powerful techniques to characterize structure and chemistry of solids at the atomic scale. The simultaneous acquisition of nanoscale chemical analysis, atomic resolution images, and diffraction patterns provides comprehensive information that other characterization tools cannot compete with. Conventional TEM typically operates under high vacuum conditions ~1.5×10^{-7} Torr [1]. However, *in situ* investigation under real-world conditions other than vacuum, such as gaseous or liquidus environment, is essential to obtain practical information [2] for materials including

catalysts, fuel cells, biological molecules, lithium ion batteries, etc. Therefore, the ability to study gas/liquid–solid interactions with atomic resolution under ambient conditions in TEM promises new insights into the growth, properties, and functionality of nanomaterials. *In situ* controlled-environment TEM (ETEM) [3, 4] enabling TEM study of specimens in ambient environment is necessary for various nanomaterial-based technologies, such as efficient energy conversion/use/storage, transportation, food production, and environmental protection [5] etc.

So far, different platforms have been developed for *in situ* ETEM observations in ambient environment and can be classified into two categories: 1) platforms with an open-cell configuration, and 2) platforms with a sealed gas/liquid cell configuration. The sealed-type ETEM using a sealed cell has various advantages over the open-cell approach. First of all, the reaction volume and the specimen are confined by electron-transparent top and bottom "windows," allowing gas/liquid to be introduced and sealed within a tiny space, and separated from the other parts of the TEM column. The resulting electron path length is on the order of a few microns [6, 7], much thinner than the opened-type approach and allowing much better resolution to observe lattice images. This is especially good for gas cell because the acceptable reaction pressures within the gas cell can equal or exceed a full atmosphere [6, 8–10] while maintaining the ability to record atomic resolution images [8–11]. Furthermore, much more rapid thermal response than standard heating holders and more rapid stabilization of specimen drift can be realized by integrating miniaturized, low mass heating devices [12], or laser heating [1] into the sealed cell. Therefore, a better control of the reaction process and the imaging experiments is achieved. An additional advantage is that the sealed-cell approach only modifies a small device on the tip of a TEM sample holder, thus can be used in any normal TEM without modifications to any other parts of a TEM. The cost of performing ETEM studies using the sealed-cell approach is typically a tiny fraction of the cost of a dedicated ETEM using open-type approach, because the latter requires modifications to the whole column. Thereby the sealed-cell approach allows *in situ* ETEM studies to be easily extended to many laboratories in the field. Last but not least, the sealed-cell platforms enable *in situ* ETEM characterization with the introduction of any types of volatile carbon-based electrolytes, which is impossible for open-type approach due to the high vacuum requirement inside TEM chamber.

Due to the various advantages over the open-type approach, sealed-cell approach has become the dominant way to perform ETEM studies under ambient conditions. A fast-growing number of research groups worldwide are conducting researches using this technology. This chapter discusses *in situ* ETEM studies in ambient environment by using sealed gas/liquid cells. Different designs and applications of the sealed cells for *in situ* TEM observations are summarized. Future research directions of the sealed gas/liquid cells are demonstrated for the benign development of this field.

2. Sealed gas cells

TEM is one of the most powerful techniques to characterize structure and chemistry of solids at the atomic scale. The simultaneous acquisition of nanoscale chemical analysis, atomic

resolution images, and diffraction patterns provides comprehensive information that other characterization tools cannot compete with. However, information about the structural and chemical changes under ambient conditions, especially under gaseous environment, is usually not available since conventional TEM operates under high vacuum conditions ~1.5×10^{-7} Torr [1]. For materials such as catalysts, fuel cells, and biological molecules, *in situ* investigation under real-world conditions other than vacuum is essential to obtain practical information [2]. Therefore, the ability to study gas-solid interactions with atomic resolution at ambient pressures in TEM promises new insights into the growth, properties, and functionality of nanomaterials. Significant improvements in scanning/TEM (S/TEM) technologies containing a gaseous environment have enabled now the atomic scale study during gas-solid interactions [5] with energy resolution in the sub-eV range, and sensitivity to detect single atoms [13]. *In situ* controlled-ETEM [3, 4] enabling TEM study of specimens in ambient environment is necessary for various nanomaterial-based technologies, such as efficient energy conversion/use/storage, transportation, food production, and environmental protection [5], etc.

The original designs for ETEM observations under gaseous conditions have been around for over 70 years [14] and are made available by two main kinds of methods [15]: one is the opened type, which confines the gas near the sample by means of pressure-limiting apertures and maintain the vacuum in the remaining column by a differential pumping scheme [16–19] (e.g. in 1991, Nan Yao et. al. [20] used two pole pieces to confine the gas near the sample region, for studying supported metal catalysts during catalytic process in a TEM column); the other is the sealed type, which uses a sealed gas cell [4, 7, 8, 21–24] to enclose the sample and the high-pressure gas within a tiny space. For the opened type, the pressure-limiting apertures with small holes are positioned in the objective lens in close proximity to the sample, and the differential pumping system is equipped to avoid diffusion of the gas molecules from the chamber toward other parts of TEM, especially the electron gun. Any type of specimen holder can be accepted by the opened-type ETEM. However, differential pumping ETEM has many obvious disadvantages [9], such as a long time needed to ramp up to and down from a selected temperature, difficulty of stabilizing specimen drift due to the large power consumption and heating effects of the heating unit, huge cost needed to modify the TEM column, and the long gas path (on the order of ~1 cm [2, 6, 25]) through which the electron beam must pass that limits reaction pressures to a level of about 15–20 Torr [1].

On the other hand, the sealed-type ETEM using a sealed gas cell has various advantages over the differential pumping approach. First of all, the reaction volume and the specimen are confined by electron-transparent top and bottom "windows," allowing a gas to be introduced and sealed within a tiny space, and separated from the other parts of the TEM column. The resulting gas path length is on the order of a few microns [6, 7], much thinner than the opened-type approach and allowing much better resolution to observe lattice images. Consequently, the acceptable reaction pressures within the gas cell can equal or exceed a full atmosphere [6, 8–10] while maintaining the ability to record atomic resolution images [8–11]. Furthermore, much more rapid thermal response than standard heating holders and more rapid stabilization of specimen drift are realized by integrating miniaturized, low mass heating devices [12] or

laser heating [1] into the sealed gas cell. Therefore, a better control of the reaction process and the imaging experiments is achieved. An additional advantage is that the sealed-gas-cell approach only modifies a small device on the tip of a TEM sample holder, thus can be used in any normal TEM without modifications to any other parts of a TEM. The cost of performing ETEM studies using the gas-cell approach is typically a tiny fraction of the cost of a dedicated ETEM using differential-pumping approach, because the latter requires modifications to the whole column. Thereby, the sealed-gas-cell approach allows *in situ* ETEM studies to be easily extended to many laboratories in the field. Due to the various advantages, sealed-gas-cell approach has become the dominant way to perform ETEM studies under gaseous environment. A fast-growing number of research groups worldwide are conducting researches using this technology.

Advances in 0D [26], 1D [27], and 2D [28–43] material fabrication technologies have enabled various forms of nanoscale materials, which increased the needs of *in situ* ETEM studies through the closed-type approach, i.e. sealed gas cells. Sealed gas cells enabled *in situ* TEM observations, thus allowing the evaluation of the effect of external stimuli including mechanical, electrical, and magnetic force on nanomaterials. Some advantages of *in situ* TEM observations with sealed gas cells are listed as follows [44]:

1. Concurrent observations of structural, morphological, and chemical changes in ambient atmosphere are enabled.

2. The same area is observed during the whole reaction process in ambient atmosphere, when sample is subjected to external stimuli.

3. Intermediate steps during reactions in the ambient atmosphere can be identified.

4. Both thermodynamic and kinetic data leading to nanomaterials synthesis or functioning in ambient atmosphere can be obtained.

5. Considerable time saving as the synthesis and characterization are performed concurrently in ambient atmosphere.

The sealed gas cells have been applied in a variety of research fields and topics, including dynamic observation of catalytic reactions [2, 8, 21, 23–45], oxidation and reduction of metals [22], interaction between materials and ionized gas [46], de/hydrogenation processes [47], biological studies [4, 7], etc. Some groups just used their newly developed sealed cells to demonstrate their properties and improved technical limits for *in situ* TEM observations [1, 9, 10, 48, 49]. These applications are discussed in details as follows.

2.1. (De)hydrogenation processes

Hydrogen storage materials are needed for hydrogen fuel, particularly in the automotive industry. To enhance the kinetics and modify the thermodynamics of hydrogenation, nanostructured hydrogen storage materials are needed and study of the *in situ* hydrogenation/ dehydrogenation process on the atomic scale is essential [47]. Using the MEMS-type sealed gas cell, Tadahiro Yokosawa et al. [47] observed the hydrogenation and dehydrogenation of Pd with a very consistent precision and a nanometer resolution, allowing a distinction between

hydrogenation behaviors of individual grains. The electron beam was found to have no disturbing influence on the determination of the (de)hydrogenation temperatures in the case of Pd, under normal working conditions and at pressures of 750 and 2400 Torr. The relationship between (de)hydrogenation and pressure fitted well with bulk experiments in which the pressure was varied. Fast determination of the hydrogenation and dehydrogenation temperatures was allowed by realizing a very fast change in temperature.

2.2. Interactions between materials and gases

In 1976, Hiroshi Fujita et. al. [50] designed and used a sealed gas cell for a 3MV-class electron microscope to observe the reaction between H_2 gas and iron, as shown in **Figure 1(a)**. After electron irradiation damage in vacuum, the secondary defects were preferentially formed around the dislocations, which were linear structures in **Figure 1(a)**. Fern-leaf-like structures were formed around individual dislocation lines when the iron foil was exposed to wet H_2 gas of ~1200 Torr for ~30 min during electron irradiation of 2×10^{19} e/sec.cm^2 in intensity, as seen in micrograph (a′), which is an enlargement of a framed part in **Figure 1(a)**. These fern-leaf-like structures were quite different from those in **Figure 1(b)**, therefore they might be some sort of Fe hydrides that were closely related to the hydrogen embrittlement of iron.
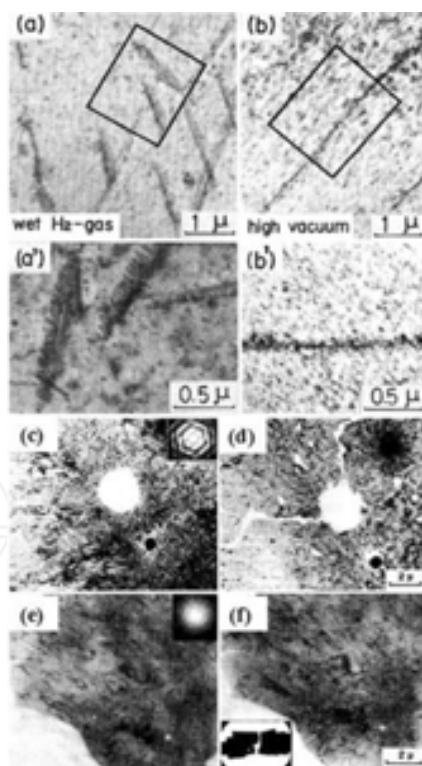

Figure 1. Reaction between wet H_2 gas and an iron foil. Micrographs (a) and (b) were taken after a heavy electron irradiation in wet H_2 gas of about 1200 Torr and a vacuum of 1×10^{-6} Torr, respectively. Micrographs (a′) and (b′) are enlargement of framed parts in (a) and (b), respectively. (c)–(d): Evaporation of 18/8 type stainless steel at 650°C in a vacuum of 1×10^{-6} Torr. (e)–(f): Evaporation of 18/8 type stainless steel at higher than 700°C in Ar-10 vol % H_2 gas of 760 Torr [50].

2.3. Suppression of specimen evaporation

The same sealed gas cell by Hiroshi Fujita et al. [50] was also used for suppression of the evaporation of specimen at high temperatures, thus decreasing the damage made by evaporation when metals and alloys were annealed at considerably high temperatures in vacuum. **Figure 1(c)–(f)** show the suppression of evaporation of 18/8 type stainless steel during annealing. The specimen (**Figure 1(c)**) was partly evaporated in a vacuum of 1×10^{-6} Torr by heating at 650°C, as seen in **Figure 1(d)**. In contrast, the evaporation of specimen was remarkably suppressed in a mixed gas of 760 Torr consisting of commercially pure Ar gas and 10 volume% H_2 gas even when the specimen was heated at high temperatures (more than 700°C). Microstructures in the specimen could be seen clearly even when a gas layer was as thick as ~100 μm, as shown in **Figure 1(e)** and **(f)**.

2.4. Oxidation and reduction of metals

Making use of the heating element and the enclosed gases, *in situ* observations of oxidation and reduction processes can be performed with sealed gas cells. **Figure 2** shows the oxidation process of a Cu thin film in a sealed gas cell designed by M. Komatsu et al. [22] in 2005. Initially, a small amount of Cu oxide formed during evaporation, as shown in the bright field image (**Figure 2(a)**) and the corresponding selected area electron diffraction pattern (**Figure 2(a′)**), respectively. Oxygen was then introduced into the cell to 9.75 Torr and the specimen was gradually heated to 470K. Cu oxide was found to preferentially nucleate on the film surface (**Figure 2(b)** and **(b′)**). As the temperature increased, Cu was oxidized to very fine oxide particles, as shown in **Figure 2(c)** and **(c′)**. After the specimen was heated to 670K, all particles changed to CuO (**Figure 2(d)** and **(d′)**). The CuO grains grew larger when the specimen temperature reached 770K (**Figure 2(e)** and **(e′)**). The reduction of CuO was also observed *in situ*, as shown in **Figure 2**. The film was gradually reheated in 9.75 Torr of H_2. As the specimen temperature was further increased, CuO was completely reduced to Cu at 670 K (**Figure 2(h)** and **(h′)**).
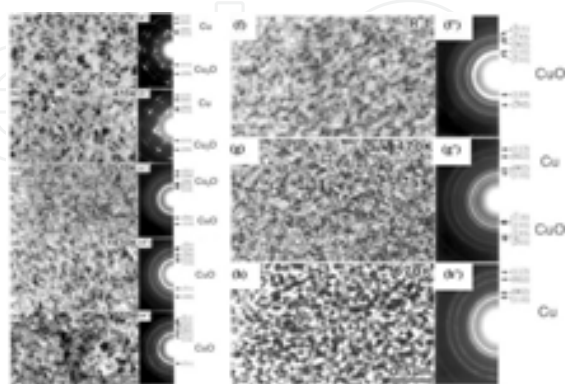

Figure 2. Successive stages of the oxide growth on a 100-nm-thick Cu thin film between room temperature and ~770K under 1.3×10^3 Pa of O_2. (a)–(e): Bright field images. (a′)–(e′): The corresponding SAEDs. Successive stages of the reduction of CuO between room temperature and ~670K under 1.3×10^3 Pa of H_2. (f)–(h): Bright field images. (f′)–(h′): The corresponding SAEDs [22].

2.5. *In situ* growth of nanostructures

In situ observation of the growth process of CuO whiskers was carried out in the same sealed gas cell by M. Komatsu et al. [22]. A series of electron micrographs show the successive stages of growth of Cu oxide whiskers in 30 Torr of O_2 (**Figure 3**). Initially, a non-uniform oxide film formed on the Cu surface, resulting to a jagged edge (**Figure 3(a)** and **(b)**). After 40s, the oxide layer stabilized with a smoother edge (**Figure 3(c)**). Then whiskers started to grow on the oxide layer gradually (**Figure 3(d)–(f)**).
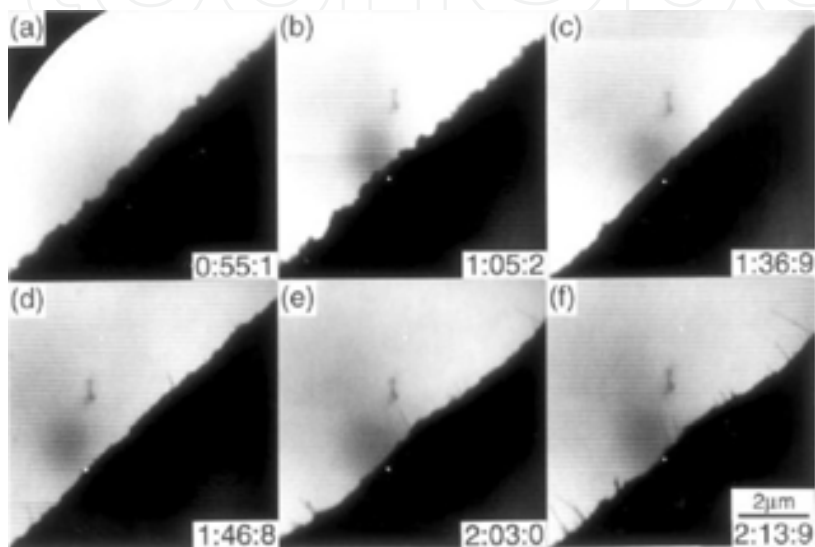

Figure 3. Successive stages of growth of Cu oxide whiskers in 30 Torr of O_2 [22].

2.6. Reactions with atomic/ionized gases

The earliest report of interactions with ionized/atomic gas induced by the electron beam of TEM was made by Li Sun et al. [46] in 2011. The enhanced electron flux could increase the concentrations of both reducing electrons and oxygen ions. Below a certain threshold, oxidization dominated the system response and resulted in accelerated interaction between silver and oxygen ions. The average size of silver grains continued to decrease, as shown in **Figure 4(c)–(f)**. At current densities of 0.44 A cm^{-2}, the silver grains were rod-shaped (**Figure 4(c), (d)**). At current densities greater than 0.65 A cm^{-2}, the silver grains reverted back to a more compact angular morphology (**Figure 4(f)**). Due to the increased oxygen fugacity associated with higher concentrations of ionized and atomic oxygen, all Ag_2O phase was further oxidized to AgO at current densities greater than 0.65 A cm^{-2}. Above 0.75 A cm^{-2}, a significant portion of noncrystalline phase existed (**Figure 4(g)**). Once the electron current density increased beyond 0.77 A cm^{-2}, new grains nucleated (**Figure 4(h)**) out of the vapor phase, exhibiting a twin structure. The reaction between the nanoparticles (NPs) and gas produced a concentration gradient around the particles that was observed as a bright ring around each silver grain. The silver oxide depletion width in the gas phase indicated a strong chemical interaction between the solid and vapor phases. The AgO vapor phase often aligned

itself into 2D sheets perpendicular to the beam that subsequently became unstable precipitate clusters of new silver grains or swept through a region randomly (**Figure 4(h)**). The competition between oxidation and electron-beam-induced reduction also provided excess heat. For significantly high fluxes of ionized oxygen, a thermal effect could induce local vaporization at the surface, and sequentially an *in situ* nanoscale reaction ion sputtering. This investigation revealed a variety of microstructural processes associated with the oxidation of Ag by atomic and ionized gas species. The electron beam was demonstrated to be an important source of both oxidation and reduction. The sealed cell approach provided an opportunity to make early observations of real-time nanoscale dynamics associated with oxidation in ionized and atomic gas, the movement of a partial pressure of a gas phase, and interactions between the condensed and vapor phases of a material. The results provided new insights into manipulating nanostructure and chemistry through ionized gas treatment and offered unique access to simulate reactions with atomic and ionized gas.
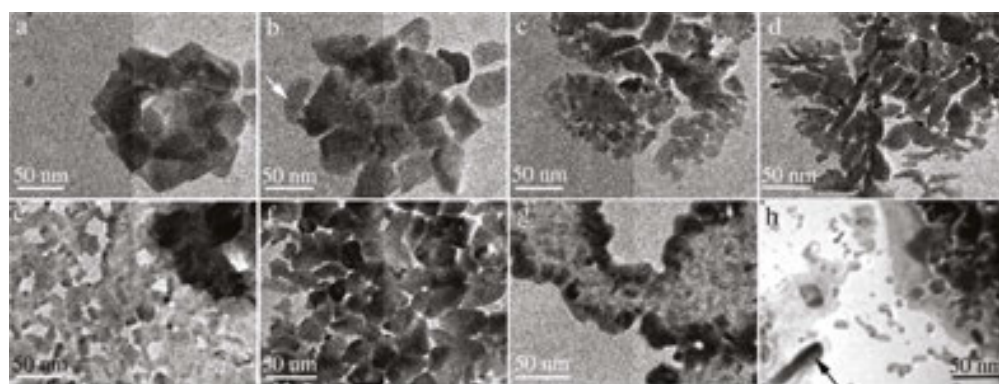

Figure 4. Microstructure of the observation area in an air-filled cell after exposure of (a) 0 s with 0.18 A cm^{-2} current density; (b) 20 s with 0.18 A cm^{-2} current density (the arrow marks a new grain); (c) 0 s with 0.44 A cm^{-2} current density; (d) 20 s with 0.44 A cm^{-2} current density; (e) 0 s with 0.66 A cm^{-2} current density; (f) 20 s with 0.66 A cm^{-2} current density; (g) 20 s with 0.72 A cm^{-2} current density; and (h) 20s with 0.8 A cm^{-2} current density (the arrow marks the vertical alignment of the AgO vapor phase) [46].

2.7. Dynamic observation of catalysts and catalytic reactions

One of the earliest attempts to observe a catalyst in a sealed gas cell was reported by Parkinson et al. [21] in 1989. Using a narrow-gap, sealed gas cell and a 400-kV TEM, images of the crystal lattice of ceria (0.31 nm) were recorded under flowing nitrogen gas at 20 Torr. Structural information of chemical significance became discernible at ~0.3 nm, which offered real hope of carrying out fundamental dynamic studies of the activation, reaction, and passivation of gas/solid systems at close to the atomic level.

Seventeen years later, the atomic-scale *in situ* observations of catalysts were performed by S. Giorgio et al. [23], during a chemical reaction. For the first time, Au and Pd clusters supported on Ti0$_2$ and amorphous carbon were observed with a sealed gas cell with the resolution of (111) lattice fringes. Initially, an Au cluster in vacuum was strongly contaminated, but the contamination disappeared while the faceting and the crystalline lattice were visible in the cluster

after circulation of H_2 at a pressure of 3 Torr at room temperature. The cluster was completely faceted after annealing until 350°C in the same reducing atmosphere, then cooling down to room temperature.

The resolution of *in situ* observation of catalysts was improved by a novel MEMS-type nanoreactor in 2008 [8]. More importantly, the nanoreactor facilitated the direct observation of Cu nanocrystal growth and mobility on a sub-second time scale at a higher temperature (500°C) and higher gas pressure (900 Torr of H_2). The *in situ* TEM images showed atomic lattice fringes in the Cu nanocrystals with spacing of 0.18 nm, attesting the spatial resolution limit of the system. The system of Cu nanocrystals on a ZnO support is commonly used as catalyst for methanol synthesis and for conversion of hydrocarbons in fuel cells. Also, it is a prototype example of the industrially important group of 3d transition metal catalysts. The catalyst was heated in the H_2 atmosphere to the maximum operation temperature of 500°C. ZnO crystallites with diameters of 20–100 nm appeared in the precursor with facetted, compact shapes (**Figure 5(a)**). The CuO appeared as smaller patches of more irregular shapes at the edges of
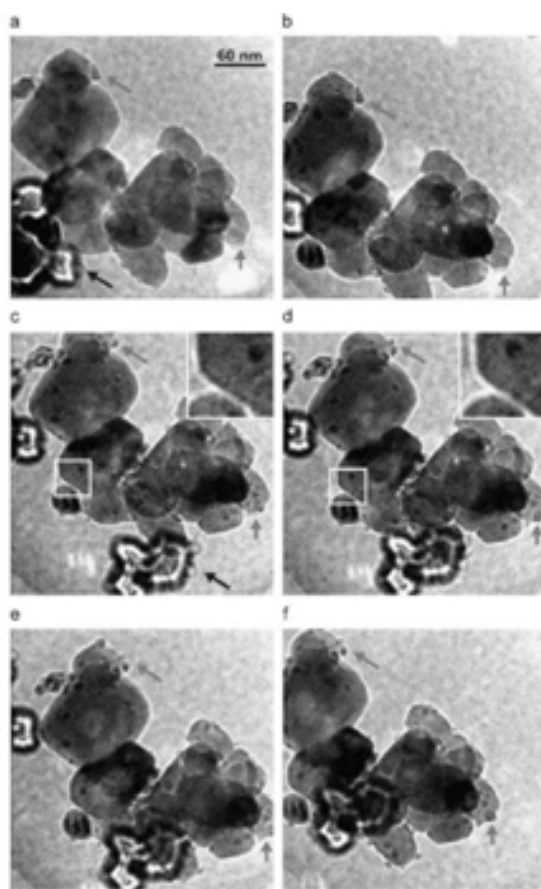

Figure 5. Image sequences of the Cu nanocrystal growth and mobility on ZnO. Nanocrystals (darker contrast) form from CuO precursors (blue arrows) during heating from room temperature to 500°C in 900 Torr H_2. After growth, nanocrystals can exhibit transient mobility (white square). Crystallites on the opposite window are seen out of focus (black arrows in (a) and (c)). The frames are recorded at (a) room temperature, (b) 260°C, (c) 330°C, (d) 365°C, (e) 410°C, and (f) 500°C. All frames are averaged over four consecutive images. The exposure time for each image is 0.145 s (color online) [8].

ZnO. As temperature increased to ~260°C, the CuO patches broke up into several particles with diameters of 5–10 nm (**Figure 5(b)–(e)**). The state of the nanocrystals was inferred from atomic-resolution TEM images during exposure to 900 Torr H_2 at 500°C. Atomic lattice fringes were clear in both the brighter ZnO support crystallites and the darker Cu nanocrystals (**Figure 6(a)**). Lattice fringes with spacings of 0.21 and 0.18 nm could be recorded in the nanocrystals [24], corresponding to (111) and (200) planes of Cu, identified by Fourier transform (**Figure 6(b)**) of the TEM image.
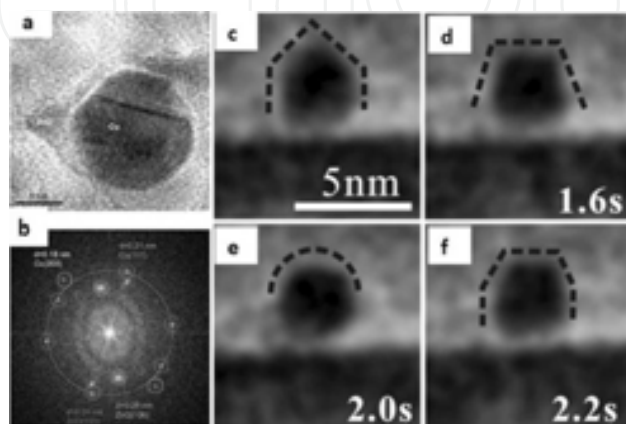

Figure 6. A representative HRTEM image of the Cu/ZnO catalyst during exposure to 900 Torr hydrogen at 500°C. (a) The image displays lattice fringes of a twinned Cu nanocrystal and of the ZnO support. (b) A Fourier transform of (a). The bright dots represent sets of lattice fringes. Their lattice spacing corresponds to the distance to the origin and reveals the crystallographic identity. The large, red circle corresponds a spacing of 0.21 nm. The smallest, resolved lattice spacing is 0.18 nm. (c)–(f) [2]: *In situ* TEM images of the nanoparticulate gold catalyst supported on TiO_2 recorded sequentially. The time shown in the lower right-hand corners of (d)–(f) correspond to intervals measured from the time at which (c) was recorded (color online) [8].

One year later, the MEMS-type sealed gas cell developed by Tadahiro Kawasaki et. al. [2] was applied for *in situ* TEM observations of a gold nanoparticulate catalyst supported on TiO_2. One percent CO in dry air was introduced to react with O_2 to form CO_2 on the catalyst surface. **Figure 6(c)–(f)** show the sequential morphologies of the gold NP. The shape of the gold particle changed markedly over a short period of time, such as the 0.4 s interval between **Figure 6(d)** and **(e)** and the 0.2 s between **(e)** and **(f)**. Various facets of the gold appeared in **Figure 6(c)**, **(d)**, and **(f)**. They sometimes disappeared and the gold particle formed a spherical shape in **Figure 6(e)**. However, the lattice fringes of the gold could not be observed due to electron scattering by the high-pressure gas.

The most recent *in situ* visualization of oscillatory behavior of Pt NPs catalyzing CO oxidation was reported by S. B. Vendelbo et al. [45] in 2014. TEM image series of the Pt NPs were acquired at windows both at the entrance and exit of the reaction zone, at a rate (1–2 frames per second) faster than the rate of the reaction oscillations, to directly visualize the NPs on this timescale. Near the reaction zone entrance, the NPs had a stationary and more spherical morphology during the oscillating reaction. In contrast, near the reaction zone exit, the Pt NPs switched between spherical and facetted morphology (**Figure 7(1)**). As the CO conversion increased rapidly, Pt NPs started a gradual transformation from the more spherical shape towards a

more facetted shape. The fully facetted shape was reached within 3 s after the CO peak conversion (**Figure 7(1) III**). On decrease in the CO conversion, the NP transformed back to the more spherical shape (**Figure 7(1) IV**) and retained that shape until the CO conversion rose steeply again. Thus, the individual NPs near the exit from the reaction zone underwent oscillatory and reversible shape changes with a temporal frequency matching the oscillations in reaction power, indicating that the oscillatory CO conversion and the dynamic shape change of the Pt NPs were coupled. To address the mechanism governing the oscillatory reaction, the state of the Pt NPs was examined at the atomic scale (**Figure 7(2) (c)–(e)**). The spacing of crystalline lattice planes and the uniform contrast across the projected image of the NPs were consistent with metallic Pt. The combined high-resolution TEM and DFT analyses indicated that the Pt surfaces remained in the metallic state under the present conditions. Time-resolved series of high-resolution TEM images show that in the more spherical state, the Pt NPs were terminated by close-packed (111) planes, more open (110) planes and step sites (**Figure 7(2) (a), (c), (e)**), while for the more facetted state, the NPs were terminated by extended (111) planes as well as a reduced abundance of higher index terminations and steps (**Figure 7(2) (b), (d)**).
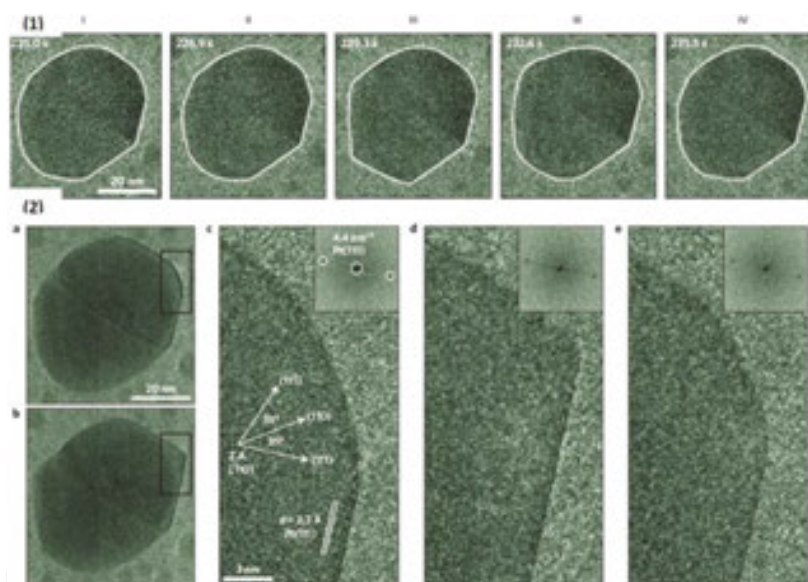

Figure 7. (1) Time-resolved TEM images of a Pt NP at the gas exit of the reaction zone. (2) Atomic-scale visualization of the dynamic refacetting of a Pt NP during the oscillatory CO oxidation. Time-resolved high-resolution TEM images of a Pt NP at the gas exit of the reaction zone. The gas entering the reaction zone is 1.0 bar of CO:O$_2$:He at 4.2%:21.0%: 74.8% and nanoreactor temperature is 727K. (a)–(e): The TEM images showing the more spherical shape (a, c, e) and the more facetted shape (b, d), during the oscillatory reaction. Fast Fourier transforms included as insets in (c)–(e) reveal a lattice spacing corresponding to the Pt(111) lattice planes. The orientation of the observed Pt(111) lattice fringes is consistent with the superimposed crystal lattice vectors and zone axis (color online) [45].

Apart from the homemade sealed gas cells above, commercial MEMS-type sealed gas cells have also been applied to *in situ* studies of catalysts. The membrane-type heating chip manufactured by Hummingbird Scientific (Lacey, WA, USA) provided a temperature controllable reaction platform for oxidation reactions of cobalt NPs with flowing oxygen (0.2 sccm), while ramping temperature from 150 to 250°C and 250 to 350°C at ~5°C/s [25]. **Fig-**

ure 8(a) shows the time-lapse images of three selected Co particles. The metallic cobalt core could shrink with a unidirectional retraction front (**Figure 8(aI)**) and a sweeping retraction front (**Figure 8(aII)**). In projection, the residual metallic puddle was faceted, which was likely shaped by the faceted hollow shell (**Figure 8(aIII)**). The quantification of the volume trajectory of the metallic core (**Figure 8(d)**) shows that the metallic core volume started to rapidly decrease when temperature reached 250°C. After the first volume-decreasing phase, volume shrinkage dwelled for a short period of time at the first plateau (① in **Figure 8(b)**). Then a second rapid decreasing phase initiated with a lower volume shrinkage rate (**Figure 8(b)**). The metallic core was finally eliminated, but at an even slower volume shrinking rate. The particle's oxide shell was in contact with other particles with upper and lower right boundaries open.
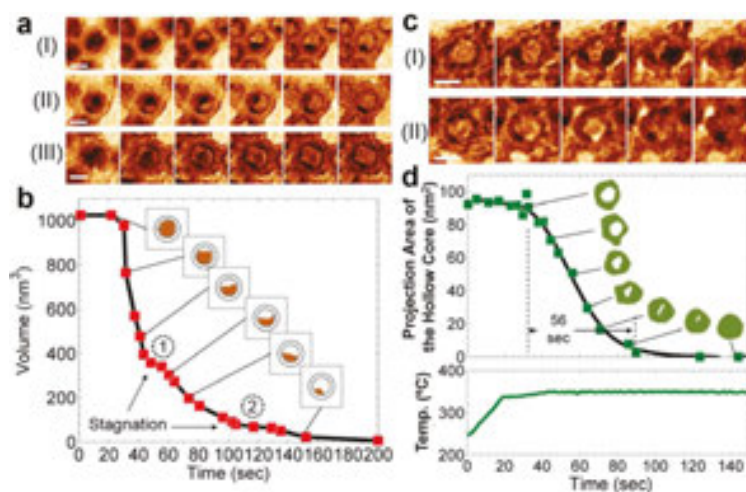

Figure 8. *In situ* heating of cobalt NPs in flowing oxygen. (a) Real-time reaction dynamics of the Kirkendall effect. (b) Metallic core volume trajectory of particle I in (a). ① and ② mark two diffusion stagnation plateaus. (c) Restructuring of the hollow oxide structure at 250–350°C in flowing oxygen. (d): Hollow core volume trajectory of particle I in (c). Scale bar is 10 nm [25] (color online).

2.8. Biological studies

The sealed gas cells encapsulated specimens in a thin gas layer, preventing specimens from destruction as in vacuum. Therefore, the sealed gas cells have also been widely applied into biological studies. This section will discuss the biological applications of the sealed gas cells for *in situ* TEM observation.

The first application of sealed gas cells in biology was reported by H. G. Heide in 1962 [4]. For organic specimens, it is necessary to prevent carbon removal from increasing to a rate higher than the rate of contamination, which would destroy the specimen. A rapid dehydration of the specimen can be prevented if unnecessary heating is avoided even at pressures of 100–200 Torr, which was proved by TEM pictures of small water droplets in air at 100 Torr. It was possible to prevent carbon removal in the specimen if H_2, He, N_2, or Ar instead of air was used at this pressure and the illuminated area was reduced to ~2 μm diameter with the double condenser.

In 2001, an *in situ* sealed gas cell was used to study the reduction of Cr (VI) by bacterium (*Shewanella oneidensis*) by T. L. Daulton et al. [7]. Bacteria from rinsed cultures were placed directly in the gas cell and examined under 97.5 Torr pressure of air saturated with water vapor, showing rod-shaped morphology typical of flagellated and non-spore-forming species (**Figure 9**). Cells remained plump/hydrated while the EPS retained moisture and appeared as a continuous capsule surrounding the cells. However, damage to the cells was observed within minutes of electron-beam exposure, arising from the primary destruction of weak Van der Waals biomolecular bonds. Direct *in situ* TEM imaging revealed two distinct populations of *S. oneidensis* in the cultures: bacteria exhibiting low image contrast (**Figure 9(a)**, **(c)**) and bacteria encrusted/impregnated with electron-dense particles (**Figure 9(b)**, **(d)**). Further examination of the encrusted bacteria showed that their gram-negative, cell envelope was electron dense (**Figure 9(d)**) and appeared darkest along the perimeter where the electron path length was the greatest. The cell envelopes of non-encrusted cells produced very low image contrast as compared to encrusted bacteria. The increase in contrast indicated that the cell envelope was saturated with absorbed elements of heavy mass, such as Cr. The binding of heavy elements in the cell envelope was associated with Cr reduction.
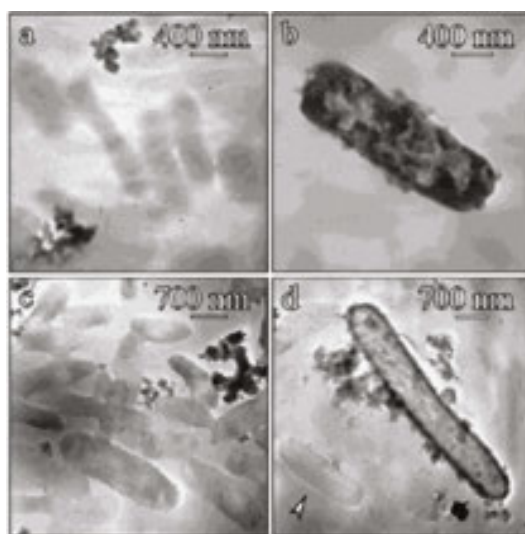

Figure 9. *S. oneidensis* imaged in the environmental cell at 100 Torr: bacteria exhibiting low contrast in bright field EC-TEM imaging (a, c), and bacteria encrusted/impregnated with electron dense particulates (b, d). The arrowhead in panel (d) points to a low contrast bacterium in the same field of view as a bacterium with electron dense particulates, illustrating the dramatic contrast difference. The low-contrast, diffuse background, best seen in panel (a), represents the extracellular polymeric substances that surround the cells [7].

2.9. *In situ* investigations on cladding materials

Cladding is the outer layer of the fuel rods, preventing radioactive fission fragments from escaping the fuel into the coolant and contaminating it. Exposures to irradiation, temperature changes, and stresses may induce microstructural changes, and ultimately result in failure of the cladding. It is thus essential to use *in situ* TEM to observe microstructural changes at the nanoscale dynamically, for predicting the performance of cladding in-service and during

storage, understanding the dominant processes related to these changes and their consequences. In 2012, a sealed gas cell developed by K. Hattar et al. [51] was used to investigate the radiation tolerance of potential Generation IV cladding materials and the degradation mechanisms in Zr-based claddings of importance for dry storage. Examination of a Zircaloy foil enclosed by top and bottom windows (**Figure 10(a)**) showed deterioration of resolution due to expected additional scattering of electrons by the 5-μm-thick air, after initial scattering by the foil. Despite loss in resolution, prominent features of the foil that were previously observed under vacuum still remained visible. After annealing at 300°C for over 15 min, negligible changes in the Zircaloy morphology occurred (**Figure 10(b)**). Following the 15-min annealing at 300°C, the temperature of the gas cell was raised to 600°C and a dramatic morphology change within the sample was observed almost instantaneously (**Figure 10(c–d)**).
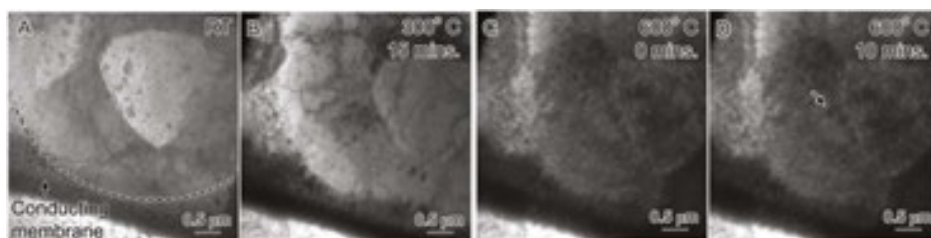

Figure 10. Images of Zircaloy lamella at nominally atmospheric pressure. (a) Initial structure. (b) 15 min at 300°C, (c) 600°C, and (d)600°C after 10 min [51].

The same device was applied to study hydride formation in Zirlo™ cladding material [12] recently. The formation of hydrides, their dissolution, and re-precipitation, is particularly important for long-term dry storage of currently used fuel assemblies, as the size, shape, and orientation of hydrides play a strong role in the mechanical properties of spent claddings. During *in situ* observation, hydrogen was introduced and maintained at a pressure of 330 Torr. The temperature was then increased at a rate of 1°C/s to approximately 400°C, and held for 90 min. **Figure 11(a)** and **(b)** show a comparison between the microstructures of the Zirlo™ prior to annealing and during later stages of annealing. The disappearance of microstructural features (arrow 1) and the formation of a new grain (arrow 2) are evident. The region around the new grain (**Figure 11(c)**) and the analysis of diffraction information (**Figure 11(d)**) indicated the formation of either ε-ZrHx (x > 1.8) or γ-ZrH. These results show that *in situ* environmental heating TEM can be applied to study this mechanism at the nanoscale in order to verify predictive material models.

3. Sealed liquid cells

Conventional TEM is not compatible with studies of electrochemical energy storage processes, but the development of TEM holders and sealed liquid cell (SLC) platforms encapsulating thin liquid layers promise *in situ* imaging and spectroscopy of electrochemical processes [52, 53]

(e.g. electrodeposition [54] and dendrite growth [55]) on the nanoscale [56–58], by incorporating electrodes [54, 59] in a liquid environment. One major application of SLCs for *in situ* TEM observation is for lithium ion battery(LIB) research. Unlike ex situ studies, which involve unexpected reactions due to the removal of the particles from their native and reactive environment [60], *in situ* TEM electrochemical characterization will mimic the true environment in a commercial LIB cell. The *in situ* liquid TEM has allowed quantitative analysis of processes (e.g. NP growth from solution [61–63]), and direct observation of beam-sensitive systems (including macromolecular complexes [64, 65], soft materials [66, 67]) and of processes that span from the electrochemical deposition of metals [54, 55], to growth of different nanostructures [61, 62, 68–71]. Now it gains growing attention for LIB research.

Apart from nanostructured anodes/cathodes, the development of platforms enabling *in situ* TEM electrochemical characterization is also required by various other aspects of LIB research. For example, one of the most well-known reactions at the electrode/electrolyte interface is the formation of the solid-electrolyte interphase (SEI), which is a reaction product of mixed composition formed on high-voltage anodes (e.g. Li metal or graphite-lithium intercalation compounds) or cathodes, by electrochemical reduction or oxidation of the electrolyte [72], respectively. The study of the SEI layer requires the use of commonly used LIB electrolytes (volatile carbonate-based solution), the ability to monitor the changes in SEI layer with cycling, time or temperature, and probes having sufficient spatial resolution to detect a reaction product layer of a few nm thick. All of these requirements make ex situ characterization inappropriate for the study of SEI, since the SEI layer is highly sensitive to moisture, air, and other kinds of contaminations [73]. The importance and critical need to develop platforms enabling *in situ* TEM electrochemical characterization of LIBs are thus obvious. Furthermore, the detailed understanding in dendritic growth of lithium metal on the electrode also requires such *in situ* TEM platforms, because the dendritic growth of lithium metal on the electrode can lead to short-circuit and thus battery failure [73].
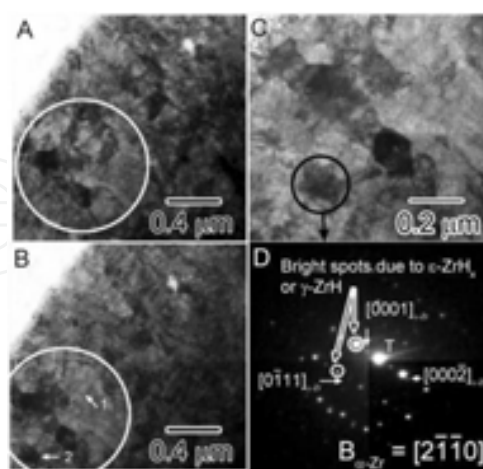

Figure 11. (a) and (b) Overview of images before the start of *in situ* experiment, and after 72 min at 400°C in H$_2$ atmosphere, (c) zoomed-in image of the region of interest around arrow 2 in (b), and (d) shows the superimposition of two diffraction patterns obtained from the circled dark grain shown in (c), one of the parent α-Zr phase (diffraction spots of weaker intensity) and the other is consistent with a face-centered tetragonal hydride phase [12].

Typical commercially available Li-ion batteries usually use carbonate-based liquids as electrolytes, such as diethyl carbonate (DEC), dimethyl carbonate (DMC) mixed with ethylene carbonate (EC), etc. To enable *in situ* TEM characterization of electrochemical reactions in real lithium ion batteries, sealing those volatile liquids inside a sufficiently narrow channel for electron transmission is a wise option. The SLC platforms enable *in situ* electrochemical characterization with any types of electrolytes with a sealed-cell configuration, thus promoting the potential use of volatile carbon-based electrolytes for LIB research. One of the first TEM SCLs was created by F.M. Ross et al. [54, 74] to study Cu electro-deposition during TEM imaging. This SLC platform sealed the aqueous electrolyte by assembling two silicon chips with thin silicon nitride membranes in a face-to-face configuration. This flip-chip approach allows imaging chemical reactions in liquids with high spatial resolution [54, 57, 58, 62, 75] with different membranes of silicon nitride, silicon dioxide, or polymer, such that it has been adopted in various studies, including cell imaging [76–78] and NP synthesis [58] in solutions. For example, electrochemical deposition of polycrystalline Au [75], anisotropic electrodeposition of nickel nanograins [79], and electrochemical growth of single crystal lead dendrites through nucleation, aggregation, alignment, and attachment of randomly oriented small grains [80] were imaged by using electrochemical SLCs.

To date, large progress has been made on fabrication and testing of the design features (including sealing, assembly, alignment, etc.) of SLCs [81], which opens the opportunity to address key questions on the electrode-electrolyte interfaces in native liquid environments, e.g. Kyong Wook Noh et al. [82] captured cyclic formation and dissolution of solid-electrolyte interphase at a Sn electrode in commercial liquid. Due to the reduced length scale of the electrodes, limited electrolyte volume, low current measurements [83], high vapor pressure of commercial electrolytes, and low contrast of lithium during TEM imaging through the membrane window, the application of SLCs as *in situ* electrochemical TEM cells for LIB research is still a great challenge and very limited. The application of sealed liquid cells for *in situ* TEM electrochemical characterization of lithium ion batteries are discussed as follows.

To track the lithiation process and elucidate the lithiation mechanism, the following techniques can be used: morphological imaging, electron diffraction [84, 85], energy-dispersive X-ray (EDX), and electron energy loss spectroscopy (EELS). Morphological imaging cannot give chemical information [60], and diffraction spots are quickly obscured in thicker liquid films. Moreover, lithium scatters electrons so weakly that elastic imaging is challenging and EDX signal for lithium has a much too low energy for detection. EELS offers chemical fingerprints (core-loss EELS) and electronic structure information (valence EELS), but EELS of Li in liquid will be degraded by multiple scattering events in thick liquids [86] and the lithium K-edge (~54 eV) cannot be distinguished from many transition metal (e.g. Fe [87]) edges and the superimposed bulk plasmon of the thick liquid films, which makes the majority of Li-edge spectroscopy to be ex situ [88] and core-loss EELS of the lithium practically impossible in a liquid cell. Therefore, valence EELS is the best way to interrogate electronic structure and detect the state of lithiation of battery electrodes in SLCs, because valence EELS provides strong signals due to large scattering cross-sections and low background from the liquid (the electronic structure shift usually occurs at energies below ~6–7 eV where the electrolyte is transparent and stable

[60]). The spatial resolution of valence EELS is ultimately limited by the delocalization of the low-energy excitations [89], multiple scattering in the liquid environment, and low-dose imaging conditions, to be on the nanometer scale. Megan E. Holtz et al. [60] successfully observed the lithiation state by valence energy-filtered TEM (EFTEM) in thicker liquid layers than commonly allowed by core-level spectroscopy [86], probing the low-energy regime at ~1–10 eV. They employed ab initio theory to calculate optical gaps of the relevant solvated species, taking solution effects into account with a hybrid function [90] including a nonlinear description of the polarization response of the surrounding liquid. By combining electrochemistry in the TEM with valence spectroscopic imaging and theory, they identified the lithiation state of both the electrode and electrolyte during *in situ* operation. Their work demonstrated the unique ability of an *in situ* TEM SLC to observe the Li de/insertion dynamics and degradation of $LiFePO_4$ cathode in real time. The real-time evolution of individual grains and NPs of $LiFePO_4$ (cathode) [60] was studied in the native environment of a battery in a liquid cell TEM (as mentioned above). Particles (lithium-rich/poor) were observed to delithiate one at a time in a mosaic fashion, with different delithiation mechanisms in neighboring particles. Core-shell structures and anisotropic growth in different particles within the same agglomerate on the electrode were directly imaged along with the phase transformations, thanks to the *in situ* SLC design. Although they used Li_2SO_4 aqueous electrolyte due to its high abundance, less viscosity, low weight, and nontoxicity [91], volatile electrolytes could be used in their SLCs. They imaged at 5 eV with a 5 eV wide energy window [60] to track the state of lithiation (**Figure 12**). There were clear differences between the charged (**Figure 12**, right) and the discharged state (**Figure 12**, left) in both the particles and the solution in the 5 eV spectroscopic
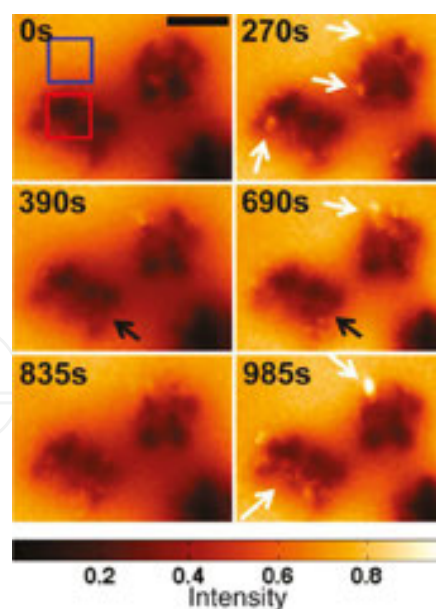

Figure 12. *In situ* charging and discharging of the cathode material $LiFePO_4$ in 0.5 M Li_2SO_4 aqueous electrolyte: the 5 eV spectroscopic EFTEM images of charging and discharging at indicated times. Scale bar is 400 nm. Bright regions are delithiated $FePO_4$ and dark regions are $LiFePO_4$. There are more bright regions of $FePO_4$ at the end of charge cycles and less during the discharges. White arrows point toward "bright" charged particles, and black arrows point toward "dark" discharged particles [60].

images. Particles showed more bright regions (corresponding to delithiated $FePO_4$) in the charged state. The cluster of particles was brighter in the charged image as marked by black arrows, especially around the edges of the cluster. The brightest particles may correspond to completely delithiated $FePO_4$, whereas the overall slight increase in intensity in the particles may indicate partially delithiated particles. On discharge, these bright regions of $FePO_4$ disappeared, transitioning back to $LiFePO_4$.

The electrochemical lithiation of Au electrode, dendritic growth of crystalline lithium, and the subsequent stripping of lithium and thinning of Li-Au layer under the applied cyclic voltammetry was observed by Zeng et al. [73], using commercial $LiPF_6$/EC/DEC electrolyte, which proved that real electrolyte of LIBS can be used in electrochemical SLCs [73]. **Figure 13 (A)−(J)** shows the sequential images representing the early stage of electrolyte decomposition, lithiation of gold electrode, and the subsequent growth and dissolution of lithium dendrites. **Figure 13 (k)** shows the corresponding applied electrical potential and measured electrical current from frame **(A)** to frame **(J)**. The thickness of Li-Au alloy did not change drastically at the later stage, as shown in **Figure 13(L)**. During stripping, the dissolution of plated lithium starts from the tip and the kink points as a reverse process of plating (**Figure 13(M)**). The formation of SEI layer on the other side of the electrode was also captured for better understanding of correlation between cyclic stability and the passivating film formed during the charge-discharge process in real LIBs. The drawback in their design was a lack of lithium metal source inside the SLC to supply the consumed lithium ions, such that the Li ion concentration in the electrolyte changed during the reaction. Adding a lithium metal source and an additional reference electrode into the SLC is necessary for direct comparison between the electrochemical processes inside a TEM column and that in real LIBs.
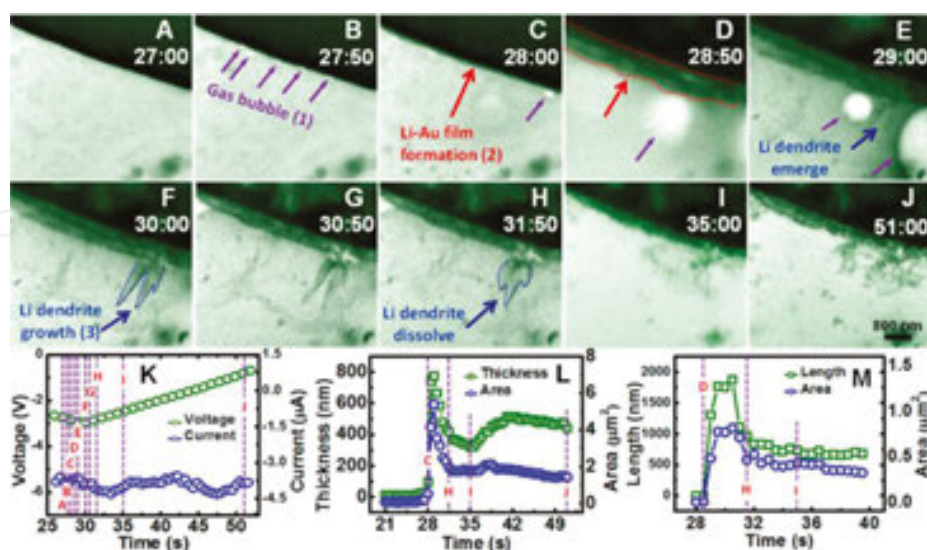

Figure 13. (A−J) Time evolution of the growth and dissolution of Li-Au alloy and lithium dendrite; (K) the corresponding applied electric potential and measured electric current from frame A to frame J; (L) plot of Li-Au layer thickness and area as a function of time; (M) dimension and area evolution of the lithium dendrite tip as a function of time during cyclic voltammetry in the voltage range of 0 to −3 V at scan rate of 0.1 V/s [73].

SLCs have also been used to study the stabilities of different electrolytes commonly used for Li-ion and Li-O$_2$ battery [92, 93]. Five different electrolytes [94], including LiAsF$_6$ salt dissolved in three different organic solvents: (1) 1,3-dioxolane (DOL), (2) DMC, (3) a mixture of DMC and EC and LiTf in dimethyl sulfoxide (DMSO), LiPF$_6$ in EC/DMC were studied. **Figure 14** shows six different time series of bright-field (BF) STEM images corresponding to the five electrolyte solutions and the EC/DMC solvent alone. To ensure that the observed lack of degradation products when imaging the LiTf:DMSO mixture was not a result of improper focus, the edge of the window was recorded as a reference. **Figure 14** shows that apart from LiTf in DMSO, all the other salt-containing solutions tested showed some evidence of degradation. It is worth to note that the degradations of the electrolytes were triggered by the imaging electrons (300 kV), instead of extra electrodes. This work shows that the electron-beam in the STEM can be used as an effective tool for evaluating stability and degradation in battery electrolytes by allowing direct visualization of the reductive decomposition of the electrolyte components, instead of postmortem analysis (chromatography) [95, 96]. This *in situ* approach can potentially be used for more rapid identification of next-generation electrolytes.
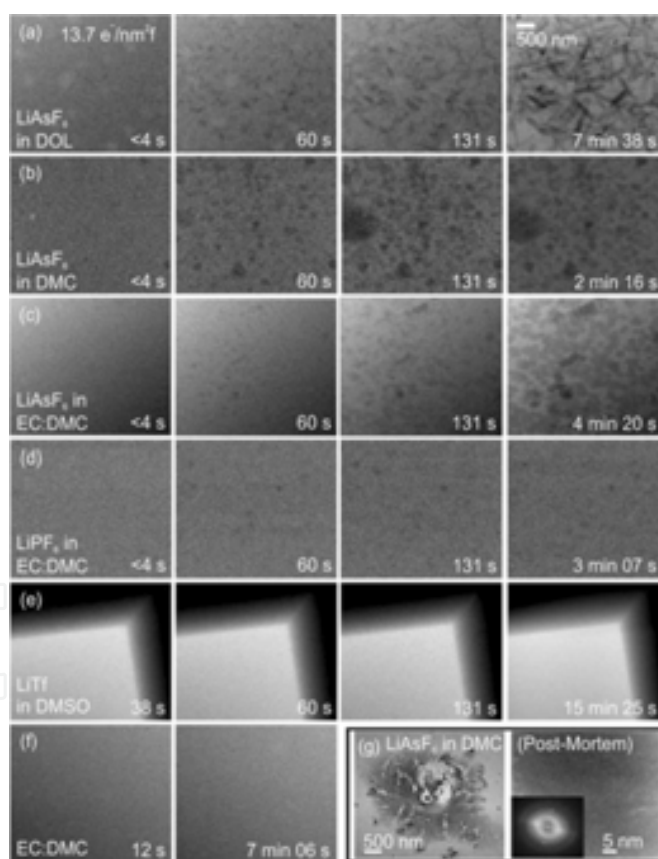

Figure 14. e⁻ beam-induced breakdown of different electrolytes upon irradiation. (a–e) Cropped BF STEM images showing the time evolution of five different electrolytes at serial exposure times. (f) Frames from a data set probing the stability of the solvent EC/DMC for the same dose conditions as above over 7 min of continuous irradiation. (g) TEM images of an irradiated area of the LiAsF6 in DMC mixture after separating and washing the Si chips for performing postmortem analysis. Low-magnification (left) and high-resolution TEM and consequent fast Fourier transform of the irradiated area shows the presence of LiF nanocrystals [94].

The lithiation and delithiation process of fully submerged electrodes is another important application of SLCs. For example, the de/lithiation process of Si NW electrodes during electrochemical testing was observed [88] by using *in situ* SLC platform and real electrolyte (as mentioned previously). The structural evolution of the Si NW upon lithiation is illustrated in **Figure 15(a)−(c)**. The pristine Cu-Si NW has an overall diameter of ~100 nm as revealed by the dark contrast in **Figure 15(a)**. The width of the Cu coating on the Si NW was measured to be ~80 nm. The lithiation of the Si nanowire immersed in the liquid electrolyte progressed in the core-shell fashion. The total diameter of the wire changed from 100 to 298 nm at 1658 s (**Figure 15(b)**) and to 391 nm at 2462 s (**Figure 15(c)**). The diameter as a function of lithiation time is plotted in **Figure 15(d)**. The increase of the diameter was quicker at the beginning of the lithiation and slowed down with the progression of the lithiation process. The lithiation behavior observed by the *in situ* SLC was also compared with that obtained based on the open-cell configuration in their study. For the case of SLC, the Si NW was fully immersed in the liquid electrolyte so that the insertion of lithium ions into Si was from all possible directions at the same time. The lithiation of the single nanowire proceeded in a core-shell mode with a uniform shell thickness along the axial direction of the whole nanowire, providing a global view of the response of the whole single NW with lithium insertion. However, for the open-cell configuration the lithium ion source was only in contact with the end of the Si nanowire, leading to the sequential lithiation process of the nanowire in only one direction.
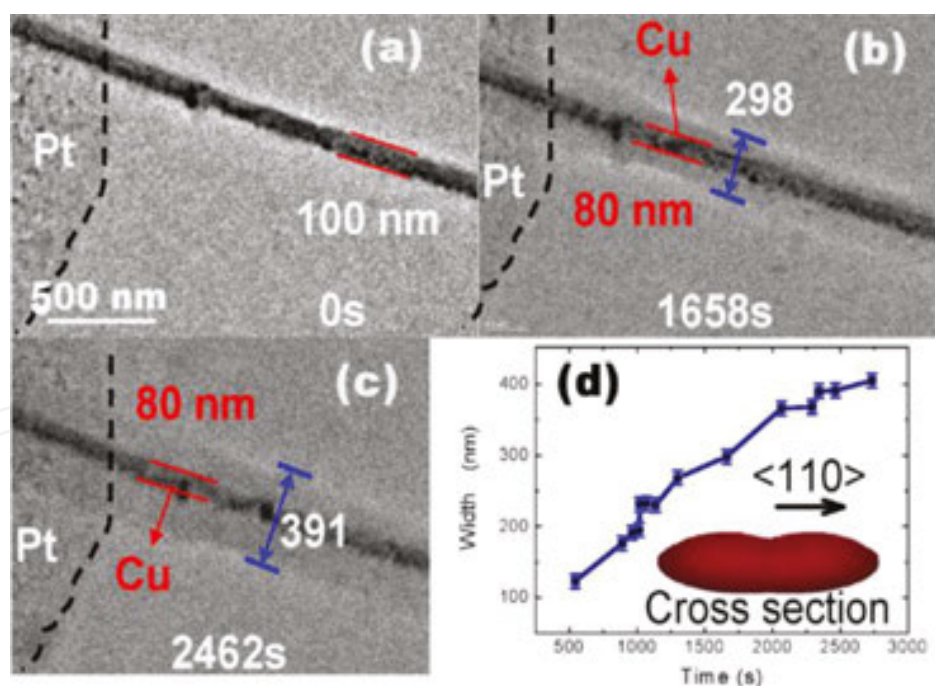

Figure 15. *In situ* liquid-cell TEM observation of the lithiation of the Cu-coated Si (Cu-Si) NW. (a) TEM image showing the pristine state of the Cu-Si NW at 0 s; (b) core-shell formation of the Cu-Si NW during lithiation at 1658 s; (c) TEM image of the Cu-Si NW at 2462 s; (d) plotted width changes of the NW as a function of time. Note that, in all images from a to c, the Pt contact region is labeled by the black lines in the left of the image. The inset in panel c illustrating the cross-sectional image after anisotropic swelling of the Si nanowire upon lithium insertion with maximum volume expansion along the <100> direction [88].

Apart from Si NW electrodes, Si NPs as electrode material were also studied by using G-SLC [56, 97], which showed that the very first lithiation at the Si-electrolyte interface had the strong orientation dependence favoring the <110> directions, but then the Li diffusion occurred isotropically after passing the initial stage regardless of the NP size. This indicated that the rate-limiting diffusion barrier is at Si-electrolyte interfaces instead of within Si or at the interfaces between lithiated and unlithiated regions. The orientation-dependent initial lithiation phenomenon was evidenced by HRTEM images as well as electron diffraction analyses, as shown in **Figure 16**. For the representative three Si NPs (whose original diameters are 34, 83, and 103 nm), their morphological and dimensional changes along <110>, <111>, and <100> directions were monitored. The selected-area electron diffraction patterns (the left ones in **Figure 16** (**a-c**)) indicated that all of the three Si NPs were single-crystalline with <110> zone axes. The lithiation progressed predominantly along <110> directions, leading to the anisotropic volume expansion along the same crystal orientations, as indicated by the white arrows in **Figure 16** (**a–c**).
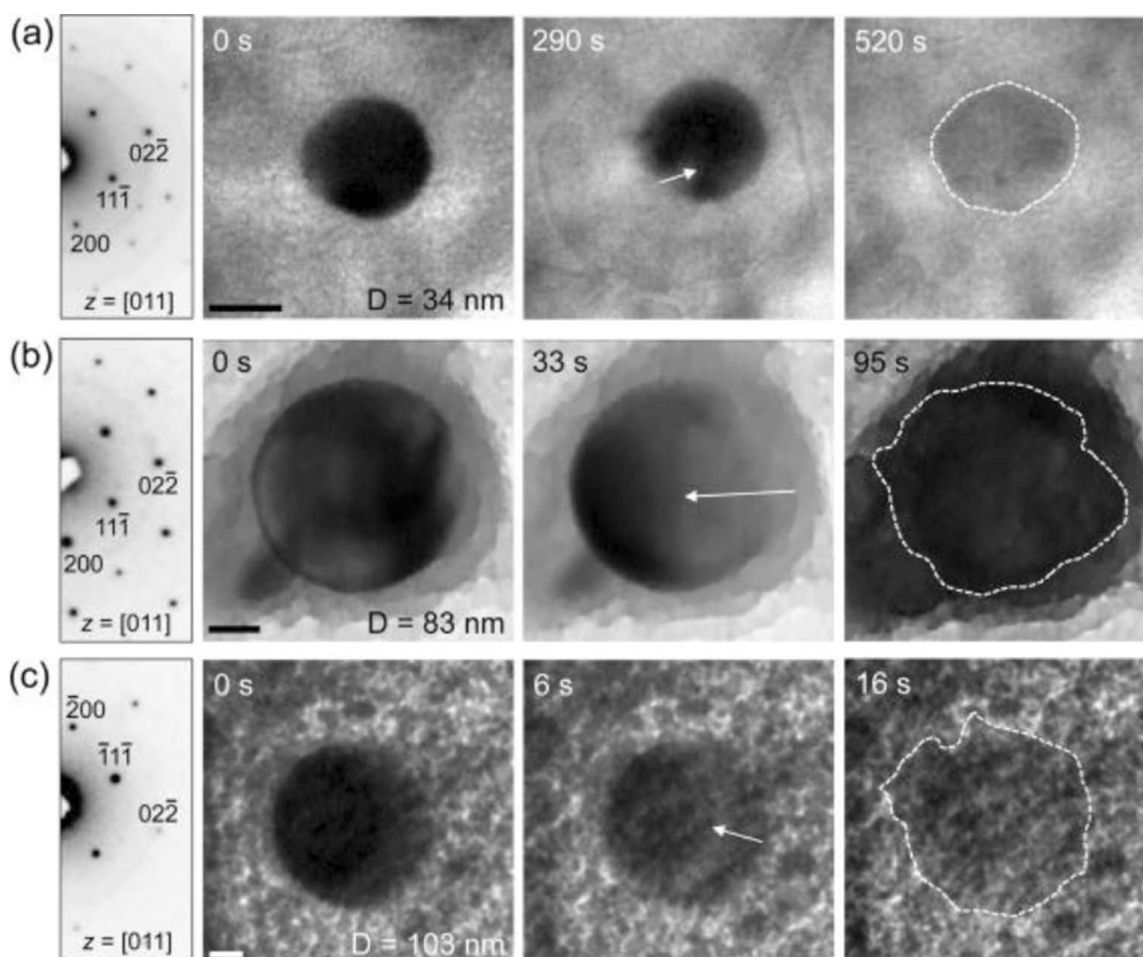

Figure 16. Morphological and dimensional changes of Si NPs analyzed by GLC-TEM during the course of lithiation: (a–c) Time series bright-field TEM images of the Si NPs with initial diameters of 34, 83, and 103 nm, respectively. The white arrows indicate the Si<110> directions. The SA-EDPs in (a–c) indicate crystalline nature of the pristine Si NPs and their crystallographic orientations along <110> zone axes. The scale bars in (a–c) are 20 nm [97].

Based on the above discussions, the major research achievements to date in applications of SLCs for *in situ* TEM electrochemical characterization of LIBs are highlighted as follows:

1. The stabilities and degradation mechanisms of commercial electrolytes commonly used for Li-ion and Li-O$_2$ battery were studied [94], providing reference for future choices on electrolytes.

2. The lithiation and delithiation process of fully submerged electrodes, such as Si NW electrodes [88, 98], Sn electrodes [82], and Si NPs [97], during electrochemical testing were observed by using *in situ* SLC platform and real electrolyte.

3. The electrochemical lithiation process, such as dendritic growth of crystalline lithium [60], stripping of lithium [60], SEI layer formation [99, 100], etc., were observed in real time with nanoscale resolution during electrochemical charge and discharge [60] using commercial electrolyte [73].

4. Summary and future research directions

In sum, sealed gas cells for *in situ* ETEM observation and sealed liquid cells for *in situ* TEM electrochemical characterization of LIBs have been reviewed in this article. Sealed cells have various advantages over the opened-type approach, thus becoming the dominant way to perform ETEM studies under gaseous/liquid environment. However, improvements are still needed in the following aspects for the benign development of this technology.

For sealed gas cells, thermal expansion/contraction and the consequent sample drift need to be minimized during *in situ* ETEM observation. The key to realize this is to improve ways of heating the sample. Localized heating sources such as laser or infrared light can be used for this purpose. Furthermore, the gas path length for electrons to go through the sealed gas cells needs to be decreased, possibly by better designs of the cell configurations. For example, if the heater can be integrated into the window instead of hanging out in the middle of the cell, the thickness of the spacer can be decreased such that a shorter gas path length is accomplished. Moreover, the pressure limit within the sealed gas cell should be increased, so that this technique can be applied to increasingly more fields of study. This can be achieved by various approaches: 1) since the major concern for limiting the pressure is the mechanical strength of the windows, either modifying the manufacturing process of the windows or replacing the current material with new ones may work well; 2) the configurations of the windows can be improved to withstand a higher pressure. For example, a single window with a large surface area is easier to break under high pressure, compared with several smaller windows distributing evenly. Last but not least, the solid-gas reactions need to be controlled and monitored better by developing ways to measure the parameters of the sample inside the cell more precisely. The direct approach to achieve this goal is to integrate measurement devices, such as nanoscale thermometers and pressure gauges into the sealed gas cells. The indirect way is to use chemical analysis techniques to reflect temperature and pressure changes. For example, the drift of EELS peak positions can be used to tell the temperature change.

For sealed liquid cells, TEM characterization of lithium through a liquid is challenging because lithium is a weak elastic scatterer and multiple scattering from the liquid could dominate the signal, resulting to a poor spatial resolution and contrast. Consequently, the spatial resolution and contrast needs to be enhanced. The future research direction is to improve SLC designs for better spatial resolution, which can be realized by decreasing the thickness of the liquid layer, redesigning the electrode configuration, utilizing alternative viewing window materials, employing different electrolytes, controlling electron dose, optimizing spacer thickness, etc. With an improved spatial resolution, various new research frontiers, including defect structure within SEI layer during (de)lithiation process, can be explored by using SLCs in TEM, rendering it the most promising technique for *in situ* electrochemical characterization of LIBs.

Author details

Fan Wu[*] and Nan Yao

*Address all correspondence to: fanwu@princeton.edu

Princeton Institute for the Science and Technology of Materials (PRISM), Princeton University, USA

References

[1] Mehraeen S, McKeown JT, Deshmukh PV, Evans JE, Abellan P, Xu P, et al. A (S)TEM gas cell holder with localized laser heating for in situ experiments. Microscopy and Microanalysis. 2013;19:470–8.

[2] Kawasaki T, Ueda K, Ichihashi M, Tanji T. Improvement of windowed type environmental-cell transmission electron microscope for in situ observation of gas-solid interactions. Review of Scientific Instruments. 2009;80:113701.

[3] Heide H. Elektronenmikroskopie von Objekten unter Atmosphärendruck oder unter Drucken, welche ihre Austrocknung verhindern. Naturwissenschaften. 1960;47:313–7.

[4] Heide HG. Electron microscopic observation of specimens under controlled gas pressure. The Journal of Cell Biology. 1962;13:147–52.

[5] Jinschek JR. Advances in the environmental transmission electron microscope (ETEM) for nanoscale in situ studies of gas-solid interactions. Chemical Communications. 2014;50:2696–706.

[6] Hansen TW, Wagner JB. Catalysts under controlled atmospheres in the transmission electron microscope. ACS Catalysis. 2014;4:1673–85.

[7] Daulton TL, Little BJ, Lowe K, Jones-Meehan J. In situ environmental cell–transmission electron microscopy study of microbial reduction of chromium(VI) using electron energy loss spectroscopy. Microscopy and Microanalysis. 2001;7:470–85.

[8] Creemer JF, Helveg S, Hoveling GH, Ullmann S, Molenbroek AM, Sarro PM, et al. Atomic-scale electron microscopy at ambient pressure. Ultramicroscopy. 2008;108:993–8.

[9] Allard LF, Overbury SH, Bigelow WC, Katz MB, Nackashi DP, Damiano J. Novel MEMS-based gas-cell/heating specimen holder provides advanced imaging capabilities for in situ reaction studies. Microscopy and Microanalysis. 2012;18:656–66.

[10] Yaguchi T, Suzuki M, Watabe A, Nagakubo Y, Ueda K, Kamino T. Development of a high temperature-atmospheric pressure environmental cell for high-resolution TEM. Journal of Electron Microscopy. 2011;60:217–25.

[11] de Jonge N, Bigelow WC, Veith GM. Atmospheric pressure scanning transmission electron microscopy. Nano Letters. 2010;10:1028–31.

[12] Rajasekhara S, Hattar KM, Tikare V, Dingreville RPM, Clark B. Hydride formation in cladding materials studied via in-situ environmental heating transmission electron microscopy. 2012.

[13] Rose HH. Historical aspects of aberration correction. Journal of Electron Microscopy. 2009;58:77–85.

[14] Marton L. La microscopie electronique des objets biologiques. Bulletin de l'Academie de Belgique Classe des Sciences (5). 1937;28:672–5.

[15] Tanaka N, Usukura J, Kusunoki M, Saito Y, Sasaki K, Tanji T, et al. Development of an environmental high-voltage electron microscope for reaction science. Microscopy. 2013;62:205–15.

[16] Baker RTK, Harris PS. Controlled atmosphere electron microscopy. Journal of Physics E: Scientific Instruments. 1972;5:793.

[17] Butler EP. In situ experiments in the transmission electron microscope. Reports on Progress in Physics. 1979;42:833.

[18] Boyes ED, Gai PL. Environmental high resolution electron microscopy and applications to chemical science. Ultramicroscopy. 1997;67:219–32.

[19] Sharma R. Design and applications of environmental cell transmission electron microscope for in situ observations of gas–solid reactions. Microscopy and Microanalysis. 2001;7:494–506.

[20] N. Yao GES, R. A. Kemp, D. C. Guthrie, R. D. Cates, C. M. Bolinger. Environmental cell TEM studies of catalyst particle behavior. In: Bailey G, editor. 49th Annual Conference of EMSA. San Francisco: San Francisco Press; 1991. p. 1028–9.

[21] Parkinson GM. High resolution, in-situ controlled atmosphere transmission electron microscopy (CATEM) of heterogeneous catalysts. Catal Lett. 1989;2:303–7.

[22] Komatsu M, Mori H. In situ HVEM study on copper oxidation using an improved environmental cell. Journal of Electron Microscopy. 2005;54:99–107.

[23] Giorgio S, Sao Joao S, Nitsche S, Chaudanson D, Sitja G, Henry CR. Environmental electron microscopy (ETEM) for catalysts with a closed E-cell with carbon windows. Ultramicroscopy. 2006;106:503–7.

[24] Creemer JF, Helveg S, Kooyman PJ, Molenbroek AM, Zandbergen HW, Sarro PM. A MEMS reactor for atomic-scale microscopy of nanomaterials under industrially relevant conditions. Microelectromechanical Systems, Journal of. 2010;19:254–64.

[25] Xin HL, Niu K, Alsem DH, Zheng H. In situ TEM study of catalytic nanoparticle reactions in atmospheric pressure gas environment. Microscopy and Microanalysis. 2013;19:1558–68.

[26] Gao M, Chen X, Pan H, Xiang L, Wu F, Liu Y. Ultrafine SnO_2 dispersed carbon matrix composites derived by a sol–gel method as anode materials for lithium ion batteries. Electrochimica Acta. 2010;55:9067–74.

[27] Gbordzoe S, Kotoka R, Craven E, Kumar D, Wu F, Narayan J. Effect of substrate temperature on the microstructural properties of titanium nitride nanowires grown by pulsed laser deposition. Journal of Applied Physics. 2014;116:4310.

[28] Wu F, Rao SS, Prater JT, Zhu YT, Narayan J. Tuning exchange bias in epitaxial Ni/MgO/TiN heterostructures integrated on Si(1 0 0). Current Opinion in Solid State and Materials Science. 2014;18:263

[29] Rao S, Prater J, Wu F, Nori S, Kumar D, Narayan J. Integration of epitaxial permalloy on Si (100) through domain matching epitaxy paradigm. Current Opinion in Solid State and Materials Science. 2013;18:1–5.

[30] Rao SS, Prater J, Wu F, Shelton C, Maria J-P, Narayan J. Interface magnetism in epitaxial $BiFeO_3$-$La_{0.7}Sr_{0.3}MnO_3$ heterostructures integrated on Si (100). Nano letters. 2013;13:5814–21.

[31] Rao SS, Prater JT, Wu F, Nori S, Kumar D, Yue L, et al. Positive exchange bias in epitaxial permalloy/MgO integrated with Si (100). Current Opinion in Solid State and Materials Science. 2014;18:140–6.

[32] Singamaneni SR, Prater J, Wu F, Narayan J. Interface magnetism of two functional epitaxial ferromagnetic oxides integrated with Si (100). APS March Meeting Abstracts. 2014;1:1249

[33] Singamaneni SR, Prater J, Wu F, Nori S, Kumar D, Yue L, et al. Positive exchange bias in epitaxial permalloy/MgO integrated with Si (100). APS March Meeting Abstracts. 2014;1:1254

[34] Wu F. Planar defects in metallic thin film heterostructures: North Carolina State University; 2014.

[35] Bayati M, Molaei R, Wu F, Budai J, Liu Y, Narayan R, et al. Correlation between structure and semiconductor-to-metal transition characteristics of VO_2TiO_2/sapphire thin film heterostructures. Acta Materialia. 2013;61:7805–15.

[36] Wu F, Narayan J. Controlled epitaxial growth of body-centered cubic and face-centered cubic Cu on MgO for integration on Si. Crystal Growth & Design. 2013;13:5018–24.

[37] Molaei R, Bayati R, Wu F, Narayan J. A microstructural approach toward the effect of thickness on semiconductor-to-metal transition characteristics of VO_2 epilayers. Journal of Applied Physics. 2014;115:4311.

[38] Wu F, Zhu YT, Narayan J. Grain size effect on twin density in as-deposited nanocrystalline Cu film. Philosophical Magazine. 2013;93:4355–63.

[39] Lee YF, Wu F, Narayan J, Schwartz J. Oxygen vacancy enhanced room-temperature ferromagnetism in Sr_3SnO/c-YSZ/Si (001) heterostructures. MRS Communications. 2014;4:7–13.

[40] Wu F, Zhu YT, Narayan J. Macroscopic twinning strain in nanocrystalline Cu. Materials Research Letters. 2013;2:63–9.

[41] Lee YF, Wu F, Kumar R, Hunte F, Schwartz J, Narayan J. Epitaxial integration of dilute magnetic semiconductor Sr_3SnO with Si (001). Applied Physics Letters. 2013;103:2101.

[42] Wu F, Wen HM, Lavernia EJ, Narayan J, Zhu YT. Twin intersection mechanisms in nanocrystalline fcc metals. Materials Science and Engineering: A. 2013;585:292–6.

[43] Gupta N, Singh R, Wu F, Narayan J, McMillen C, Alapatt GF, et al. Deposition and characterization of nanostructured Cu2O thin-film for potential photovoltaic applications. Journal of Materials Research. 2013;28:1740–6.

[44] Sharma R. Experimental set up for in situ transmission electron microscopy observations of chemical processes. Micron (Oxford, England : 1993). 2012;43:1147–55.

[45] Vendelbo SB, Elkjær CF, Falsig H, Puspitasari I, Dona P, Mele L, et al. Visualization of oscillatory behaviour of Pt nanoparticles catalysing CO oxidation. Nat Mater. 2014;13:884–90.

[46] Sun L, Noh KW, Wen J-G, Dillon SJ. In situ Transmission Electron Microscopy Observation of Silver Oxidation in Ionized/Atomic Gas. Langmuir. 2011;27:14201–6.

[47] Yokosawa T, Alan T, Pandraud G, Dam B, Zandbergen H. In-situ TEM on (de)hydrogenation of Pd at 0.5–4.5 bar hydrogen pressure and 20–400°C. Ultramicroscopy. 2012;112:47–52.

[48] Vendelbo SB, Kooyman PJ, Creemer JF, Morana B, Mele L, Dona P, et al. Method for local temperature measurement in a nanoreactor for in situ high-resolution electron microscopy. Ultramicroscopy. 2013;133:72–9.

[49] Alan T, Yokosawa T, Gaspar J, Pandraud G, Paul O, Creemer F, et al. Micro-fabricated channel with ultra-thin yet ultra-strong windows enables electron microscopy under 4-bar pressure. Applied Physics Letters. 2012;100:—.

[50] Hiroshi F, Masao K, Isao I. A universal environmental cell for a 3MV-class electron microscope and its applications to metallurgical subjects. Japanese Journal of Applied Physics. 1976;15:2221.

[51] Hattar K, Rajasekhara S, Clark BG. In situ TEM ion irradiation and atmospheric heating of cladding materials. MRS Online Proceedings Library. 2012;1383:null-null.

[52] Liu XH, Zhang LQ, Zhong L, Liu Y, Zheng H, Wang JW, et al. Ultrafast Electrochemical Lithiation of Individual Si Nanowire Anodes. Nano Letters. 2011;11:2251–8.

[53] Huang JY, Zhong L, Wang CM, Sullivan JP, Xu W, Zhang LQ, et al. In situ observation of the electrochemical lithiation of a single SnO2 nanowire electrode. Science. 2010;330:1515–20.

[54] Williamson MJ, Tromp RM, Vereecken PM, Hull R, Ross FM. Dynamic microscopy of nanoscale cluster growth at the solid–liquid interface. Nat Mater. 2003;2:532–6.

[55] White ER, Singer SB, Augustyn V, Hubbard WA, Mecklenburg M, Dunn B, et al. In situ transmission electron microscopy of lead dendrites and lead ions in aqueous solution. ACS Nano. 2012;6:6308–17.

[56] Yuk JM, Park J, Ercius P, Kim K, Hellebusch DJ, Crommie MF, et al. High-resolution EM of colloidal nanocrystal growth using graphene liquid cells. Science. 2012;336:61–4.

[57] de Jonge N, Ross FM. Electron microscopy of specimens in liquid. Nat Nano. 2011;6:695–704.

[58] Zheng H, Smith RK, Jun Y-w, Kisielowski C, Dahmen U, Alivisatos AP. Observation of single colloidal platinum nanocrystal growth trajectories. Science. 2009;324:1309–12.

[59] Grogan JM, Bau HH. The nanoaquarium: a platform for in situ transmission electron microscopy in liquid media. Journal of Microelectromechanical Systems. 2010;19:885–94.

[60] Holtz ME, Yu Y, Gunceler D, Gao J, Sundararaman R, Schwarz KA, et al. Nanoscale imaging of lithium ion distribution during in situ operation of battery electrode and electrolyte. Nano Letters. 2014;14:1453–9.

[61] Woehl TJ, Evans JE, Arslan L, Ristenpart WD, Browning ND. Direct in situ determination of the mechanisms controlling nanoparticle nucleation and growth. Acs Nano. 2012;6:8599–610.

[62] Liao H-G, Cui L, Whitelam S, Zheng H. Real-Time Imaging of Pt3Fe Nanorod Growth in Solution. Science. 2012;336:1011–4.

[63] Woehl TJ, Park C, Evans JE, Arslan I, Ristenpart WD, Browning ND. Direct observation of aggregative nanoparticle growth: kinetic modeling of the size distribution and growth rate. Nano Lett. 2014;14:373–8.

[64] Evans JE, Jungjohann KL, Wong PCK, Chiu P-L, Dutrow GH, Arslan I, et al. Visualizing macromolecular complexes with in situ liquid scanning transmission electron microscopy. Micron (Oxford, England : 1993). 2012;43:1085–90.

[65] Mirsaidov UM, Zheng H, Casana Y, Matsudaira P. Imaging protein structure in water at 2.7 nm resolution by transmission electron microscopy. Biophysical Journal. 2012;102:L15-L7.

[66] Huang T-W, Liu S-Y, Chuang Y-J, Hsieh H-Y, Tsai C-Y, Wu W-J, et al. Dynamics of hydrogen nanobubbles in KLH protein solution studied with in situ wet-TEM. Soft Matter. 2013;9:8856–61.

[67] Proetto MT, Rush AM, Chien M-P, Abellan Baeza P, Patterson JP, Thompson MP, et al. Dynamics of soft nanomaterials captured by transmission electron microscopy in liquid water. Journal of the American Chemical Society. 2014;136:1162–5.

[68] Evans JE, Jungjohann KL, Browning ND, Arslan I. Controlled growth of nanoparticles from solution with in situ liquid transmission electron microscopy. Nano Letters. 2011;11:2809–13.

[69] Zheng H, Claridge SA, Minor AM, Alivisatos AP, Dahmen U. Nanocrystal diffusion in a liquid thin film observed by in situ transmission electron microscopy. Nano Lett. 2009;9:2460–5.

[70] Jungjohann KL, Bliznakov S, Sutter PW, Stach EA, Sutter EA. In situ liquid cell electron microscopy of the solution growth of Au–Pd core-shell nanostructures. Nano Letters. 2013;13:2964–70.

[71] Parent LR, Robinson DB, Cappillino PJ, Hartnett RJ, Abellan P, Evans JE, et al. In situ observation of directed nanoparticle aggregation during the synthesis of ordered nanoporous metal in soft templates. chemistry of materials. 2014;26:1426–33.

[72] Aurbach D, Markovsky B, Levi MD, Levi E, Schechter A, Moshkovich M, et al. New insights into the interactions between electrode materials and electrolyte solutions for advanced nonaqueous batteries. Journal of Power Sources. 1999;81–82:95–111.

[73] Zeng Z, Liang W-I, Liao H-G, Xin HL, Chu Y-H, Zheng H. Visualization of electrode–electrolyte interfaces in LiPF6/EC/DEC electrolyte for lithium ion batteries via in situ TEM. Nano Letters. 2014;14:1745–50.

[74] Ross FM. Growth processes and phase transformations studied by in situ transmission electron microscopy. IBM J Res Dev. 2000;44:489–501.

[75] Radisic A, Vereecken PM, Hannon JB, Searson PC, Ross FM. Quantifying electrochemical nucleation and growth of nanoscale clusters using real-time kinetic data. Nano Letters. 2006;6:238–42.

[76] Thiberge S, Nechushtan A, Sprinzak D, Gileadi O, Behar V, Zik O, et al. Scanning electron microscopy of cells and tissues under fully hydrated conditions. Proceedings of the National Academy of Sciences of the United States of America. 2004;101:3346–51.

[77] Liu K-L, Wu C-C, Huang Y-J, Peng H-L, Chang H-Y, Chang P, et al. Novel microchip for in situ TEM imaging of living organisms and bio-reactions in aqueous conditions. Lab on a Chip. 2008;8:1915–21.

[78] de Jonge N, Peckys DB, Kremers GJ, Piston DW. Electron microscopy of whole cells in liquid with nanometer resolution. Proceedings of the National Academy of Sciences of the United States of America. 2009;106:2159–64.

[79] Chen X, Noh KW, Wen JG, Dillon SJ. In situ electrochemical wet cell transmission electron microscopy characterization of solid–liquid interactions between Ni and aqueous $NiCl_2$. Acta Materialia. 2012;60:192–8.

[80] Sun M, Liao H-G, Niu K, Zheng H. Structural and morphological evolution of lead dendrites during electrochemical migration. Sci Rep. 2013;3.

[81] Sullivan JP, Huang J, Shaw MJ, Subramanian A, Hudak N, Zhan Y, et al. Energy harvesting and storage: materials, devices, and applications In: Understanding Li-ion battery processes at the atomic-to nano-scale; Dhar NK, Wijewarnasuriya PS, Dutta AK, editors. 2010.

[82] Noh KW, Dillon SJ. Morphological changes in and around Sn electrodes during Li ion cycling characterized by in situ environmental TEM. Scripta Materialia. 2013;69:658–61.

[83] Unocic RR, Sacci RL, Brown GM, Veith GM, Dudney NJ, More KL, et al. Quantitative electrochemical measurements using in situ ec-S/TEM devices. Microscopy and Microanalysis : The Official Journal of Microscopy Society of America, Microbeam Analysis Society, Microscopical Society of Canada. 2014;20:452–61.

[84] Brunetti G, Robert D, Bayle-Guillemaud P, Rouviere JL, Rauch EF, Martin JF, et al. Confirmation of the domino-cascade model by LiFePO4/FePO4 Precession Electron Diffraction. Chemistry of Materials. 2011;23:4515–24.

[85] Wang C-M, Xu W, Liu J, Zhang J-G, Saraf LV, Arey BW, et al. In situ transmission electron microscopy observation of microstructure and phase evolution in a SnO2 nanowire during lithium intercalation. Nano Letters. 2011;11:1874–80.

[86] Holtz ME, Yu Y, Gao J, Abruna HD, Muller DA. In situ electron energy-loss spectroscopy in liquids. Microscopy and microanalysis : the official journal of Microscopy

Society of America, Microbeam Analysis Society, Microscopical Society of Canada. 2013;19:1027–35.

[87] Moreau P, Boucher F. Revisiting lithium K and iron M(2),(3) edge superimposition: the case of lithium battery material LiFePO(4). Micron (Oxford, England : 1993). 2012;43:16–21.

[88] Gu M, Parent LR, Mehdi BL, Unocic RR, McDowell MT, Sacci RL, et al. Demonstration of an electrochemical liquid cell for operando transmission electron microscopy observation of the lithiation/delithiation behavior of Si nanowire battery anodes. Nano Letters. 2013;13:6106–12.

[89] Muller DA, Silcox J. Delocalization in inelastic scattering. Ultramicroscopy. 1995;59:195–213.

[90] Ernzerhof M, Scuseria GE. Assessment of the Perdew–Burke–Ernzerhof exchange-correlation functional. The Journal of Chemical Physics. 1999;110:5029–36.

[91] Wang Y, Yi J, Xia Y. Recent progress in aqueous lithium-ion batteries. Advanced Energy Materials. 2012;2:830–40.

[92] Xu K. Nonaqueous liquid electrolytes for lithium-based rechargeable batteries. Chemical Reviews. 2004;104:4303–418.

[93] Nasybulin E, Xu W, Engelhard MH, Nie Z, Burton SD, Cosimbescu L, et al. Effects of electrolyte salts on the performance of Li–O2 batteries. The Journal of Physical Chemistry C. 2013;117:2635–45.

[94] Abellan P, Mehdi BL, Parent LR, Gu M, Park C, Xu W, et al. Probing the degradation mechanisms in electrolyte solutions for Li-ion batteries by in situ transmission electron microscopy. Nano Letters. 2014;14:1293–9.

[95] Gachot G, Grugeon S, Armand M, Pilard S, Guenot P, Tarascon J-M, et al. Deciphering the multi-step degradation mechanisms of carbonate-based electrolyte in Li batteries. Journal of Power Sources. 2008;178:409–21.

[96] Gachot Gg, Ribière P, Mathiron D, Grugeon S, Armand M, Leriche J-B, et al. Gas chromatography/mass spectrometry as a suitable tool for the Li-ion battery electrolyte degradation mechanisms study. Analytical Chemistry. 2010;83:478–85.

[97] Yuk JM, Seo HK, Choi JW, Lee JY. Anisotropic lithiation onset in silicon nanoparticle anode revealed by in situ graphene liquid cell electron microscopy. ACS Nano. 2014;8:7478–85.

[98] Layla Mehdi B, Gu M, Parent LR, Xu W, Nasybulin EN, Chen X, et al. In-situ electrochemical transmission electron microscopy for battery research. Microscopy and Microanalysis. 2014;20:484–92.

[99] Unocic RR, Sun X-G, Sacci RL, Adamczyk LA, Alsem DH, Dai S, et al. Direct visualization of solid electrolyte interphase formation in lithium-ion batteries with in situ

electrochemical transmission electron microscopy. microscopy and microanalysis. 2014;20:1029–37.

[100] Sacci RL, Dudney NJ, More KL, Parent LR, Arslan I, Browning ND, et al. Direct visualization of initial SEI morphology and growth kinetics during lithium deposition by in situ electrochemical transmission electron microscopy. Chemical Communications. 2014;50:2104–7.